

# Contrastive Learning Approach for Semi-Supervised Seismic Facies Identification Using High-Confidence Representations

Kewen Li, Wenlong Liu, Yimin Dou, Zhifeng Xu, Hongjie Duan, Ruilin Jing

**Abstract**—The manual seismic facies annotation relies heavily on the experience of seismic interpreters, and the distribution of seismic facies in adjacent locations is very similar, which means that much of the labeling is costly repetitive work. However, we found that training the model with only a few evenly sampled labeled slices still suffers from severe classification confusion, that is, misidentifying one class of seismic facies as another. To address this issue, we propose a semi-supervised seismic facies identification method using features from unlabeled data for contrastive learning. We sample features in regions with high identification confidence, and use a pixel-level instance discrimination task to narrow the intra-class distance and increase the inter-class distance. Instance discrimination encourages the latent space to produce more distinguishable decision boundaries and reduces the bias in the features of the same class. Our method only needs to extend one branch to compute the contrastive loss without extensive changes to the network structure. We have conducted experiments on two public seismic surveys, SEAM AI and Netherlands F3, and the proposed model achieves an IOU score of more than 90 using only 1% of the annotations in the F3 survey. We have made our codes and pre-trained models publicly available: [www.github.com/upcliuwenlong/CONSS](http://www.github.com/upcliuwenlong/CONSS).

**Index Terms**—Seismic Facies Identification, Semi-Supervised Learning, Seismic Interpretation, Contrastive Learning.

## I. INTRODUCTION

**S**EISMIC facies identification uses seismic wave reflection data to reveal lithology, lithofacies changes and depositional environment, which is of great significance for the exploration and development of underground sedimentary minerals such as petroleum and coal. The most accurate seismic facies distribution can be obtained from core samples and well log data, but the economic cost of well deployment and exploration is too high. In addition to this, it is also possible to manually assign seismic facies based on seismic attributes, but this is an ill-posed problem [5] and the results depend on the subjective experience of experts. With the development of machine learning, people try to carry out automatic or semi-automatic identification. Wolf et al. [1] used principal component analysis to cluster seismic attributes, Delfiner et al. [2] used discriminant functions to determine classes of

seismic facies, Liu et al. [27] achieve facies identification using a relevance vector machine (RVM) and develop a facies discriminant method based on a multikernel RVM, and Baldwin et al. [3] pioneered the use of feedforward neural networks to classify lithofacies. Coleou et al. [4] summarized and compared methods such as k-means, principal component analysis, projection tracking, self-organizing mapping, and vector quantization, and found that most traditional machine learning methods are sensitive to noise, and the identification results rarely have significant and practical geological significance. What's more fatal is that these traditional methods still require manual selection of seismic attributes, and the combination of attributes directly affects the final performance. However, due to the huge differences in different geological environments, the combination of seismic attributes selected in one area cannot be directly transferred to another area.

In recent years, deep learning technology represented by deep neural network (DNN) has been widely used in seismic interpretation, such as fault detection [16] [35] [29], salt-body delineation [11] [40], and identification of geological structural elements [13]. DNN outperform traditional machine learning methods by a large margin in many domains. The most significant advantage of DNN is the ability to adaptively learn the feature extraction and representation capabilities of the current training task from high-dimensional data, which avoids the subjective selection of seismic attributes. In addition to the above advantages, CNN also has parameter sharing and strong spatial perception capabilities, which is very suitable for dense seismic data distributed in the spatiotemporal domain. Most of the published CNN-based seismic facies identification methods [12] [30] in the past are to classify the center points of the 2D patch. The center point identification method has a large number of redundant computations during training and is extremely inefficient during prediction. From an image processing point of view, seismic facies identification is an intensive identification task, and treating it as a segmentation task [25] [33] [34] will achieve higher prediction efficiency and accuracy than classical identification tasks. Zhao et al. [17] compared a segmentation model using full inline (or crossline) slices as input with a identification model using 2D patch as input, and found that segmentation model has higher efficiency and better performance than identification model. Alaudah et al. [20] used a segmentation model based on deconvolution [7] and skip connections, and they trained the model on blocks with full seismic facies labels to predict surrounding seismic facies to solve the extrapolation task. They have open sourced

The corresponding author is Kewen Li. [likw@upc.edu.cn](mailto:likw@upc.edu.cn)

Kewen Li, Wenlong Liu, Yimin Dou, Zhifeng Xu, College of computer science and technology, China University of Petroleum (East China) Qingdao, China.

Hongjie Duan, Ruilin Jing, Shengli Oilfield Company, SINOPEC Dongying, China.

This work was supported by grants from the National Natural Science Foundation of China (Major Program, No.51991365), and the Natural Science Foundation of Shandong Province, China (No. ZR2021MF082).

the seismic data of the F3 block in the Netherlands with complete seismic facies labels, and this work will facilitate fair comparisons in the field of seismic facies identification.

Fully supervised seismic facies identification uses only annotated seismic data. DNN has a very strong ability to learn data distribution, and the more complete the data distribution, the better the performance of DNN. However, complete seismic facies annotations are usually scarce and difficult to obtain. Making full use of a large amount of unlabeled seismic data becomes the key to improving model performance. Semi-supervised learning uses a small amount of labeled data and a large amount of unlabeled data during training. Liu et al. [26] used real seismic data and fake data generated by a generative adversarial network to train a discriminator whose goal is to determine the seismic facies of real seismic data and distinguish fake data. Because of the additional data generated, they obtained better results than using only real seismic data. The semi-supervised learning method of Saleem et al. [22] is based on a pseudo-label strategy. They used a model trained on labeled seismic data to predict labels on unlabeled seismic data, and the predicted labels would be added to the training set as pseudo-labels for retraining, a training method also known as self-training. Weakly supervised methods mainly rely on some imprecise weak labels for training. The labels of the training data are similar but not identical to the strict ground-truth labels, and the cost and difficulty of obtaining weak labels is much lower than that of obtaining strict labels. The key to weakly supervised methods is how to generate these imprecise weak labels. Alaudah et al. [19] used similarity retrieval and non-negative matrix factorization [18] to obtain weak labels for slices that are similar to slices of known seismic facies. Unsupervised learning does not require labeled data. Puzyrev et al. provided the feature vector extracted by DNN to the unsupervised clustering algorithm, analyzed the clustering results in combination with seismic images, and added corresponding geological significance to each category. Recently, in order to transfer the trained model from the source domain data to the target domain with different data distribution, unsupervised deep domain adaptation methods have started to be applied to seismic facies identification. Nasim et al. [37] used DeepCORAL [9] to enforce that the inter-domain features learned by the network have similar statistics, and they applied the model trained on the Netherlands F3 survey to the Penobscot 3D seismic data in Canada.

We take into account that depositional environments tend to be continuously distributed, so the seismic reflection data at adjacent locations is also similar. Based on this point of view, we obtain a small amount of labeled data through uniform sampling, and the DNN trained with a small amount of labeled data can roughly identify seismic facies, but there is a serious classification confusion phenomenon, that is, one class of seismic facies is misclassified as another. We believe that there are two reasons for the confusion in the identification of seismic facies. First, the feature distribution learned by DNN on a small amount of labeled seismic data is biased, and it is not suitable for the remaining large amount of unlabeled seismic data. Second, the seismic features extracted by the backbone network cannot be completely linearly separated,

so it is difficult to generate appropriate decision boundaries. To address the first problem, we exploit the features of the remaining large amount of unlabeled seismic data during training. This approach does not increase the additional cost of labeling, but allows DNN to learn more general representation capabilities on a wider range of data, and the learned feature distribution will be more adaptable to the entire seismic survey. For the second problem, we encourage the feature distribution of seismic facies to satisfy the small intra-class distance and large inter-class distance. In order to make the features of different seismic facies more distinguishable, we naturally adopt the contrastive learning method [15][23][24]. Contrastive learning makes the samples of the same class (positive sample pair) closer and the samples of different classes (negative sample pair) are farther apart in the feature space by defining the loss function related to the distance metric, so that the model can learn the similarities and differences between the sample features.

There are two key factors that distinguish different contrastive learning methods, namely, the proxy task and the positive and negative sample definition strategy. Kiran et al. [36] divide the 3D seismic data into different blocks, and the seismic data slices in the same block are more similar and can be regarded as positive samples of each other. In contrast, slices of different blocks are negative samples of each other. It is obvious that they use a slice-level instance discrimination task. This method either sets a very large batchsize or requires additional data structures to store sample features in order to meet the large and consistent sample features required for contrastive learning. Moreover, their method is divided into two stages, first using contrastive learning to pre-train the backbone network, and second stage adding segmentation head to the backbone network to calculate pixel-level cross-entropy loss. Inspired by Wang et al. [38] and Liu et al. [31], our method employs a fine-grained pixel-level instance discrimination task. We select pixel-level sample features for each class of seismic facies, the features of each class of seismic facies and the central feature of the current class form a positive sample pair, and the features of other classes can be regarded as negative samples of the current class. All sample features are sampled from high-confidence regions of the prediction results. We extend a simple and effective branch of contrastive losses based on the characteristics of seismic data without requiring extensive changes to the network structure. Compared with real-world images, the distribution pattern of seismic facies is relatively fixed, and this relatively stable distribution can generate consistent sample features without relying on the momentum encoder. In addition, a large number of sample features can be obtained by using the pixel-level sample definition strategy, so the end-to-end training can be completed with only a single network without additional data structure and huge batchsize, which greatly saves hard disk space and graphics memory. By optimizing the contrastive loss and pixel-level cross-entropy loss, the proposed model trained with 1% of the labeled data can perform excellent seismic facies identification for 3D large-scale seismic data. What is even more surprising is that even if the labels are sparse, it can still achieve good results.

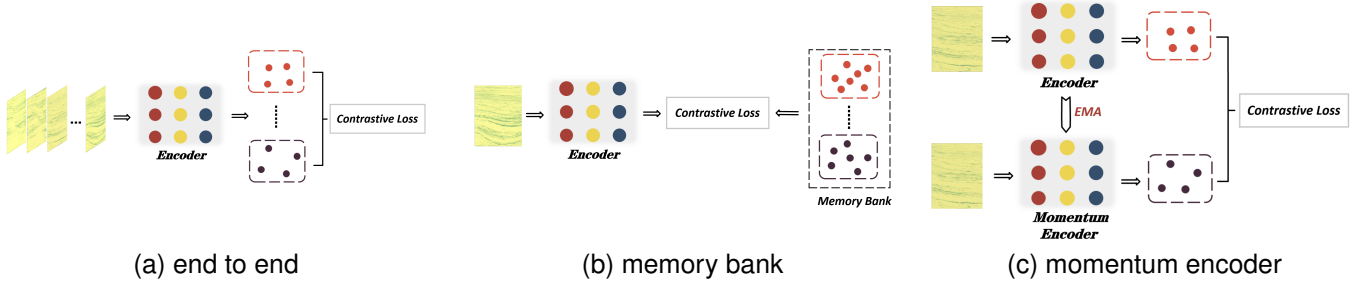


Fig. 1. (a) End-to-end architecture requires a huge batchsize to generate enough negative samples. (b) Memory bank stores samples offline. (c) Momentum encoder slowly updates samples.

In summary, the contributions of this paper are as follows:

- We propose a semi-supervised seismic facies identification method that utilizes contrastive learning to alleviate classification confusion.
- We define a pixel-level sample selection strategy that enables the model to be trained end-to-end based on a small batchsize.
- We have made our code publicly available since we believe this will be of great benefit for the geophysical community.

## II. APPROACH

### A. Network Architecture

Contrastive learning [24] requires a large number of consistent samples. In order to meet this condition as much as possible, there are three common contrastive learning frameworks, namely end-to-end, memory bank, and momentum encoder. But for seismic data, we think neither memory bank is needed to store samples nor momentum encoder is needed to slowly update samples. Compared with real-world images, seismic data has a high similarity, and the closer the location is, the higher the similarity, which will make the network generate more consistent samples. Furthermore, we use a pixel-level instance discrimination task to sample a large number of samples even within a single seismic image without using a huge batchsize and additional data structure.

We extend a representation head for contrastive learning for DeepLabv3plus [10], because contrastive learning is often not directly applied to the features extracted by the backbone, but to the features after nonlinear transformation [23]. For labeled seismic data, supervised loss is computed in the segmentation branch. For unlabeled seismic data, we screen out high-confidence regions for each class of seismic facies in the segmentation map based on the probability distribution. We sample positive and negative samples for contrastive learning in high-confidence regions of the representation map. The total loss (Eq.1) is the sum of the supervised loss and the contrastive loss.

$$\mathcal{L} = \mathcal{L}_{sup} + \mathcal{L}_{con} \quad (1)$$

### B. Supervised Loss

The segmentation branch is formalized as a nonlinear transformation  $\varphi(\mathbb{F}_{p_x, p_y}) \Rightarrow \mathbb{L}_{p_x, p_y}$ . The target of  $\varphi$  is to map

the feature  $\mathbb{F}_{p_x, p_y}$  extracted by the backbone network to the logits  $\mathbb{L}_{p_x, p_y}$  required to compute the softmax distribution, where  $(p_x, p_y)$  indicates the position in the segmentation map  $M_{seg}$ . For labeled seismic data, the pixel-level cross-entropy loss is calculated by obtaining the softmax posterior probability distribution  $\mathcal{P}$  (Eq.2). To prevent the model from being overconfident on a small amount of labeled data, we use label smoothing as regularization (Eq.3).

$$\mathcal{P}(i|\mathbb{L}_{p_x, p_y}) = \frac{e^{\mathbb{L}_{p_x, p_y}^i}}{\sum_{i=1}^{classes} e^{\mathbb{L}_{p_x, p_y}^i}} \quad (2)$$

$$\mathcal{L}_{sup} = -\frac{1}{HW} \sum_{p_y=1}^H \sum_{p_x=1}^W \sum_{i=1}^{classes} \{ \mathbb{1}[i = g_t] \cdot \log \mathcal{P}(i|\mathbb{L}_{p_x, p_y}) + \mathbb{1}[i \neq g_t] \cdot \varepsilon \log \mathcal{P}(i|\mathbb{L}_{p_x, p_y}) \} \quad (3)$$

where  $\mathbb{1}$  is the indicator function whose value is 1 when the condition is met, otherwise 0. The  $\mathbb{L}_{p_x, p_y}^i$  represents the  $i$ th component of vector  $\mathbb{L}_{p_x, p_y}$ ,  $g_t$  represents the correct seismic facies class, and  $classes$  represents the number of seismic facies classes. The dimension of  $\mathbb{L}_{p_x, p_y}$  is consistent with the number of classes. The  $\varepsilon$  is the label smoothing probability of uniform distribution and it is set to 0.1.

### C. High-confidence region

For unlabeled seismic data, although we have no way of knowing the actual seismic facies, the high-confidence region is still trustworthy. We subdivide the high-confidence region into two disjoint regions, namely the weak high-confidence region and the strong high-confidence region. We use  $t_w$  and  $t_s$  to filter the corresponding regions. The filter conditions for weak high confidence regions of class  $c$  can be described as: (a) The probability of class  $c$  is above  $t_w$  but below  $t_s$ . (b) The predicted probability of class  $c$  is the largest. These conditions can be expressed as a ternary function (Eq.4) of position  $(p_x, p_y)$  and class  $c$ :

$$mask_u^w(p_x, p_y, c) = \mathbb{1}[t_s > \mathcal{P}(i = c|\mathbb{L}_{p_x, p_y}) > t_w] \cdot \mathbb{1}[\arg \max_i (\mathcal{P}(i|\mathbb{L}_{p_x, p_y})) = c] \quad (4)$$

where  $(p_x, p_y)$  is the position in the segmentation map.

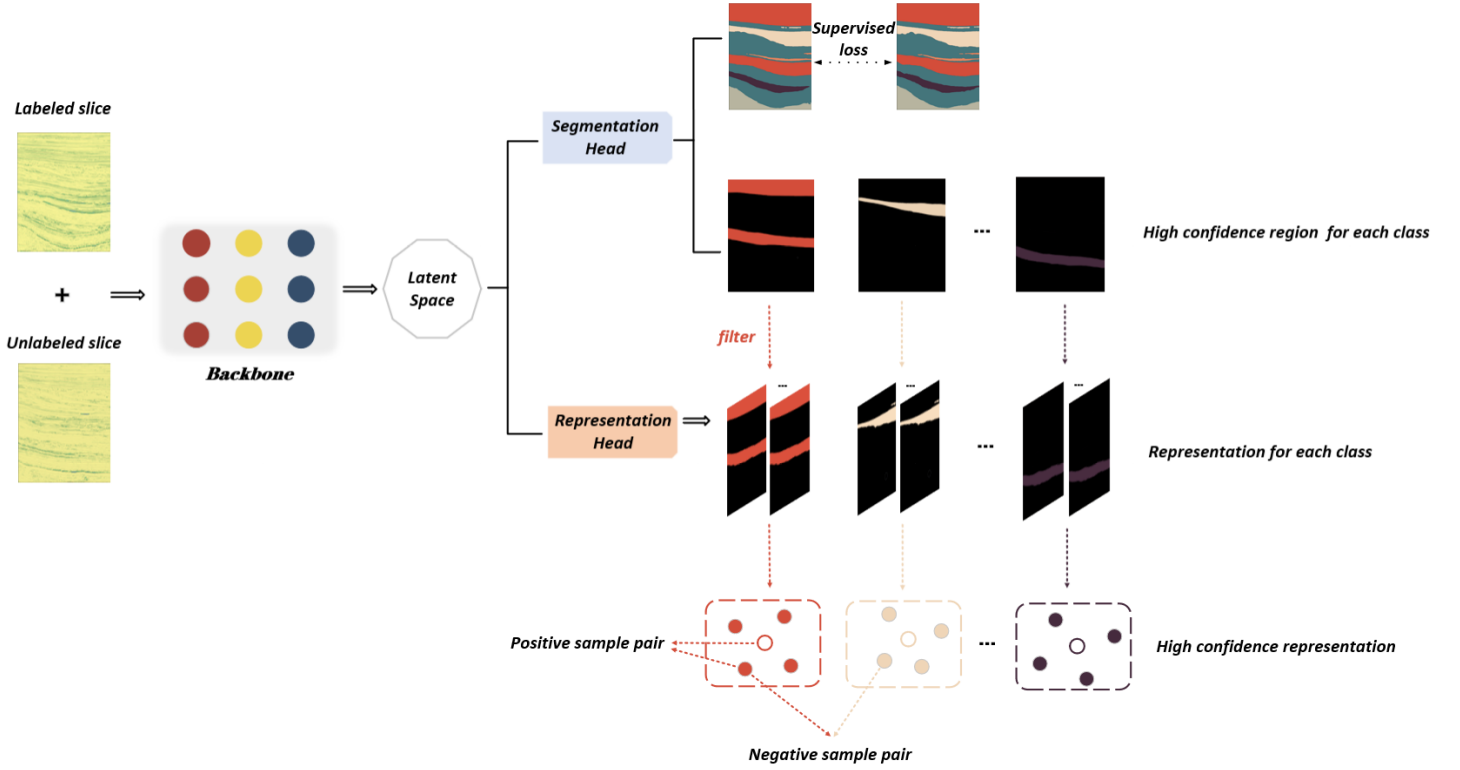


Fig. 2. Considering that the similarity of the continuous distribution of seismic facies can produce features with strong consistency, our contrastive learning does not use an additional memory bank to store negative samples, so the model can be trained end-to-end.

Similarly, the filter condition for strong high confidence regions is denoted as:

$$\begin{aligned} mask_u^s(p_x, p_y, c) = & \mathbb{1}[\mathcal{P}(i = c | \mathbb{L}_{p_x, p_y}) > t_s] \\ & \cdot \mathbb{1}[\arg \max_i (\mathcal{P}(i | \mathbb{L}_{p_x, p_y})) = c] \end{aligned} \quad (5)$$

The weak (Eq.6) or strong (Eq.7) high-confidence region for class  $c$  is composed of the following positions:

$$\mathcal{R}_u^w(c) = \{(p_x, p_y) | mask_u^w(p_x, p_y, c) = 1\} \quad (6)$$

$$\mathcal{R}_u^s(c) = \{(p_x, p_y) | mask_u^s(p_x, p_y, c) = 1\} \quad (7)$$

As for labeled seismic data, where we know the correct seismic facies, the conditions (Eq.8) used to select weak high-confidence region are different: (a) The correct class  $g_t$  is  $c$ . (b) The predicted probability of class  $c$  is the largest. (c) The probability of class  $c$  is below  $t_s$ .

$$\begin{aligned} mask_l^w(p_x, p_y, c) = & \mathbb{1}[c = g_t] \\ & \cdot \mathbb{1}[\mathcal{P}(i = c | \mathbb{L}_{p_x, p_y}) < t_s] \\ & \cdot \mathbb{1}[\arg \max_i (\mathcal{P}(i | \mathbb{L}_{p_x, p_y})) = c] \end{aligned} \quad (8)$$

The filter condition for strong high confidence regions is denoted as:

$$\begin{aligned} mask_l^s(p_x, p_y, c) = & \mathbb{1}[c = g_t] \\ & \cdot \mathbb{1}[\mathcal{P}(i = c | \mathbb{L}_{p_x, p_y}) > t_s] \\ & \cdot \mathbb{1}[\arg \max_i (\mathcal{P}(i | \mathbb{L}_{p_x, p_y})) = c] \end{aligned} \quad (9)$$

The weak (Eq.10) or strong (Eq.11) high-confidence region (Eq.10) of the labeled seismic data can be expressed as:

$$\mathcal{R}_l^w(c) = \{(p_x, p_y) | mask_l^w(p_x, p_y, c) = 1\} \quad (10)$$

$$\mathcal{R}_l^s(c) = \{(p_x, p_y) | mask_l^s(p_x, p_y, c) = 1\} \quad (11)$$

#### D. Positive and Negative Sample Definition

The output of the representation branch is the representation map  $M_{rep}$ , where at each position is a  $D$ -dimensional vector  $\mathbb{R}_{p_x, p_y}$ , and representation branch is formalized as a nonlinear transformation  $\phi(\mathbb{F}_{p_x, p_y}) \Rightarrow \mathbb{R}_{p_x, p_y}$ . The target of  $\phi$  is to map the feature  $\mathbb{F}_{p_x, p_y}$  extracted by the backbone network to the  $D$ -dimensional representation vector  $\mathbb{R}_{p_x, p_y}$  and  $D$  is set to 128. The representation map which has the same size  $H$  and  $W$  as the segmentation map, so the position  $(p_x, p_y)$  can correspond to each other. For forward propagation, we sample  $\mathcal{B}_l$  and  $\mathcal{B}_u$  of the same batchsize, so weak (Eq.12) or strong (Eq.13) high-confidence positions of the class  $c$  can be denoted as:

$$\mathcal{R}^w(c) = \mathcal{R}_u^w(c) \cup \mathcal{R}_l^w(c) \quad (12)$$

$$\mathcal{R}^s(c) = \mathcal{R}_u^s(c) \cup \mathcal{R}_l^s(c) \quad (13)$$

The query vectors for each class is derived from the weak high-confidence representations:

$$\mathcal{Q}^c = \{\mathbb{R}_{p_x, p_y} | (p_x, p_y) \in \mathcal{R}^w(c)\} \quad (14)$$

There is only one positive sample for each class, and the positive sample reflect the commonality of this class. A

positive sample of class  $c$  is the mean vector (Eq.16) of strong high-confidence representations:

$$\mathcal{S}^c = \{\mathbb{R}_{p_x, p_y} | (p_x, p_y) \in \mathcal{R}^s(c)\} \quad (15)$$

$$\mathbb{R}^{c+} = \frac{\sum_{\mathbb{R} \in \mathcal{S}^c} \mathbb{R}}{|\mathcal{S}^c|} \quad (16)$$

Negative samples of each class form a set (Eq.17) containing strong high-confidence representations of other classes:

$$\mathcal{S}^{c-} = \{\mathbb{R}_{p_x, p_y} | (p_x, p_y) \in \mathcal{R}^s(i) \wedge i \neq c\} \quad (17)$$

### E. Contrastive Loss

We encourage weak high-confidence representations of class  $c$  to be close to the class center (positive sample) and away from its negatives (Fig.3). We adopt cosine similarity (Eq.18) as a measure of the distance between two representation vectors:

$$\text{sim}(\mathbb{R}_1, \mathbb{R}_2) = \frac{\mathbb{R}_1 \cdot \mathbb{R}_2}{|\mathbb{R}_1| |\mathbb{R}_2|} \quad (18)$$

The final contrast loss is the InfoNCE [14] loss:

$$\mathcal{L}_{con} = - \frac{1}{\text{classes} \cdot Q} \sum_{c=1}^{\text{classes}} \sum_{i=1}^Q \frac{e^{\text{sim}(\mathbb{R}_i^c, \mathbb{R}^{c+})/\tau}}{e^{\text{sim}(\mathbb{R}_i^c, \mathbb{R}^{c+})/\tau} + \sum_{n=1}^N e^{\text{sim}(\mathbb{R}_i^c, \mathbb{R}^{c-})/\tau}} \quad (19)$$

where  $\mathbb{R}_i^c$  is sampled from set  $\mathcal{Q}^c$ ,  $Q$  is the sampling number.  $\mathbb{R}_n^{c-}$  is sampled from negative sample set  $\mathcal{S}^{c-}$  and  $N$  is the number of negative samples. The  $\tau$  is the temperature coefficient used to control the degree of discrimination against negative samples.

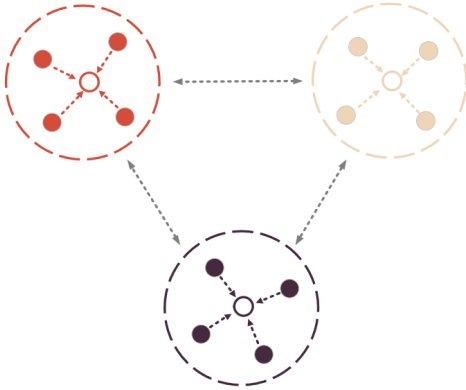


Fig. 3. The representations of the seismic facies of each class are close to the center of the respective classes, and the representations of different classes are far away from each other.

### F. Strong Data Augmentation (SDA)

We find that strong data augmentation (SDA) [32][21] is crucial for contrastive learning of unlabeled seismic data. Specifically, unlabeled seismic data are forward propagated twice. The model output pseudo labels and high-confidence

regions through first forward propagation, SDA is then applied simultaneously to unlabeled data, pseudo labels, and confidence regions, and then feeding the augmented seismic data to the network. For two slices  $X_A$  and  $X_B$  (Fig.4), the corresponding augmented slice can be expressed as:

$$SDA(X_A) = M_A \odot X_A + (1 - M_A) \odot X_B \quad (20)$$

where  $X_A$  and  $X_B$  represent slices, which can be either data slices or pseudo labels and confidence regions slices. The  $M_A$  represent mask, and different data augmentation strategies generate masks in different ways.

Interestingly, the exact opposite effect is obtained on the labeled data, where the strong data augmentation causes performance degradation on the labeled seismic data. We will discuss more specifically about SDA in the experimental session.

The complete calculation procedure of the contrastive loss is shown in algorithm (Alg.1).

---

### Algorithm 1 Contrastive Loss

---

**Input:** labeled seismic data  $\mathcal{D}_l$  and unlabeled seismic data  $\mathcal{D}_u$

**Output:**  $\mathcal{L}_{con}$

$\mathcal{L}_{con} \leftarrow 0$

$M_{seg}^u, \_ \leftarrow Model(\mathcal{D}_u)$

$M_{seg}^u, \mathcal{D}_u \leftarrow SDA(M_{seg}^u, \mathcal{D}_u)$

$\_, M_{rep}^u \leftarrow Model(\mathcal{D}_u)$

$M_{seg}^l, M_{rep}^l \leftarrow Model(\mathcal{D}_l)$

**for**  $c$  in *classes* **do**

    Get weak high-confidence region  $\mathcal{R}^w(c)$  from  $M_{seg}^u \cup M_{seg}^l$  by (Eq.12)

    Get strong high-confidence region  $\mathcal{R}^s(c)$  from  $M_{seg}^u \cup M_{seg}^l$  by (Eq.13)

**end for**

**for**  $c$  in *classes* **do**

    Get a positive sample  $\mathbb{R}^{c+}$  by (Eq.16)

    Sample negative samples  $\{\mathbb{R}_i^{c-}\}_{i=1}^N$  from  $M_{rep}^u \cup M_{rep}^l$  by (Eq.17)

    Sample query vectors  $\{\mathbb{R}_i^c\}_{i=1}^Q$  from  $M_{rep}^u \cup M_{rep}^l$  by (Eq.14)

**for**  $\mathbb{R}_i^c$  in  $\{\mathbb{R}_i^c\}_{i=1}^Q$  **do**

        Get contrastive loss  $\mathcal{L}_{con}^{\mathbb{R}_i^c}$  by (Eq.19)

$\mathcal{L}_{con} \leftarrow \mathcal{L}_{con} + \mathcal{L}_{con}^{\mathbb{R}_i^c}$

**end for**

**end for**

**Return:**  $\mathcal{L}_{con}$

---

## III. EXPERIMENT

### A. Seismic Surveys Overview

The SEAM AI survey is large 3D seismic data provided by the New Zealand government that has been manually interpreted by geologists. The survey region is in the Parihaka block of the Taranaka Basin off the northwest coast of New Zealand, and each pixel in the region is classified into one of the following six types of seismic facies:





Fig. 4. The augmented image is a superposition of the original slice  $X_A$  and another slice  $X_B$ , which preserves some of the original class pixels.

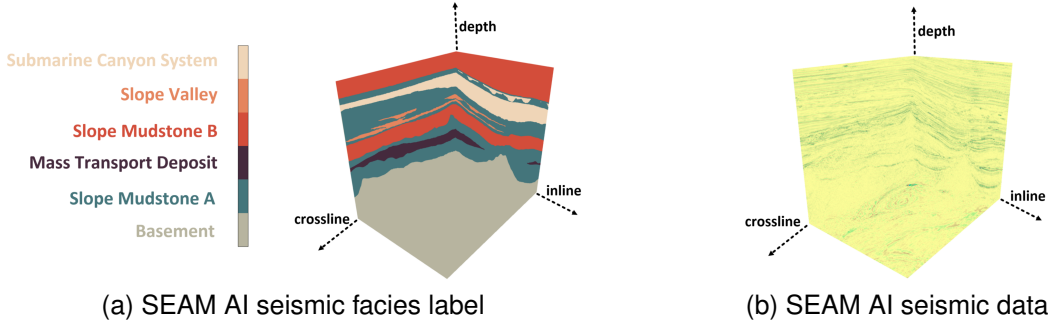


Fig. 5. The image (a) is the real distribution of seismic facies identified by different colors. The image (b) is plotted by color mapping with the intensity at each point representing (roughly) the strength of the sound-wave echo reflected back to the surface from the corresponding point in the Earth. In a seismic survey like the one that produced this image, many thousands of echoes are averaged (processed) to obtain the image value at each point.

- **Basement/Other:** Basement - Low S/N; Few internal Reflections; May contain volcanics in places.
- **Slope Mudstone A:** Slope to Basin Floor Mudstones; High Amplitude Upper and Lower Boundaries; Low Amplitude Continuous/Semi-Continuous Internal Reflectors.
- **Mass Transport Deposit:** Mix of Chaotic Facies and Low Amplitude Parallel Reflections.
- **Slope Mudstone B:** Slope to Basin Floor Mudstones and Sandstones; High Amplitude Parallel Reflectors; Low Continuity Scour Surfaces.
- **Slope Valley:** High Amplitude Incised Channels/Valleys; Relatively low relief.
- **Submarine Canyon System:** Erosional Base is U shaped with high local relief. Internal fill is low amplitude mix of parallel inclined surfaces and chaotic disrupted reflectors. Mostly deformed slope mudstone filled with isolated sinuous sand-filled channels near the basal surface.

The figure (Fig.5) show a rendering of two vertical slices and one horizontal slice.

The complete seismic facies annotation (Fig.6) of the Netherlands F3 Block was carried out by Alaudah et al [20]. This work is grounded in the geology of the region and based on the study of both the 3D seismic data and 26 well logs located within the F3 block or its vicinity.

### B. Sampling Strategy

We sampled the training data in the same way on the SEAM AI survey as well as on the Netherlands F3 survey. First we sample seismic data slices (Fig.7a) and corresponding label slices (Fig.7b) uniformly at equal intervals along the inline direction, with the sampled label slices occupying only 1% of all labels and the remaining labels used as the test set. Then

we simulate incomplete labeled seismic data by randomly discarding a portion of the labeled data (Fig.7c).

### C. Experiment Analysis

In the table (Tab.I) and table (Tab.II), *Sup* means fully supervised training using only labeled data (Fig.7b), *ConSemiSup* means contrastive semi-supervised learning using unlabeled data in addition to labeled data, *SparseConSemiSup* means labeled data is sparse (Fig.7c), and SDA is strong data augmentation. Since the data distributions are significantly different, the hyperparameters applied on the two seismic surveys are different. The results of ablation experiment of hyperparameters are given in Appendix (A). The same configuration is that we use the Adam optimizer with an suitable initial learning rate, batchsize is set to 2, and the learning rate decays to  $\frac{1}{5}$  of the previous learning rate after every 4 epochs. For the semi-supervised model,  $Q$  is set to 128, and the number of negative samples  $N$  is set to 128.

We report the performance of all model on the test set in the table. On the SEAM AI survey, our contrastive semi-supervised method with SDA improves the MIOU score of the baseline model by 5.21 points, and our method maintains a 5.11 point advantage even when the slices are sparsely labeled. On the Netherlands F3 survey, even though the baseline model achieves a high iou score of 87.37, our method still improves the score by 3.46 points.

It is worth noting that if we do not use SDA, the contrastive semi-supervised model will not work and perform worse than the baseline model. In other words, SDA is required for our semi-supervised method. However, if SDA is added to the fully supervised method, it gives very little performance boost to the model or even degrades the performance of the model.

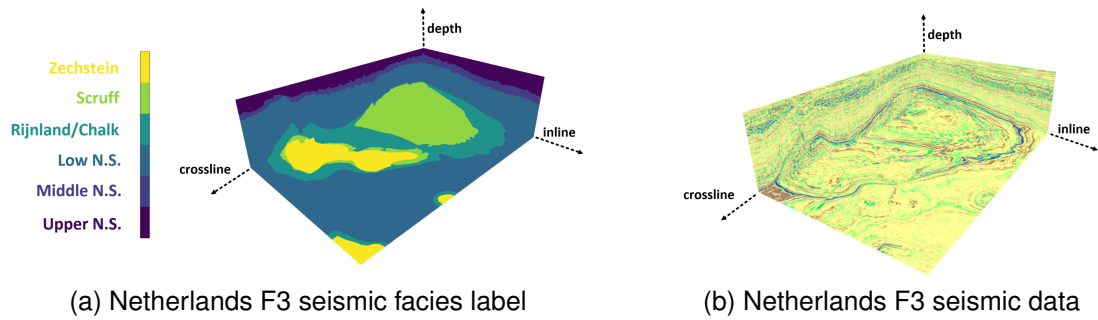


Fig. 6. The F3 survey contains six different seismic facies, and the distribution of seismic facies in the depth direction is simpler compared to SEAM AI survey.

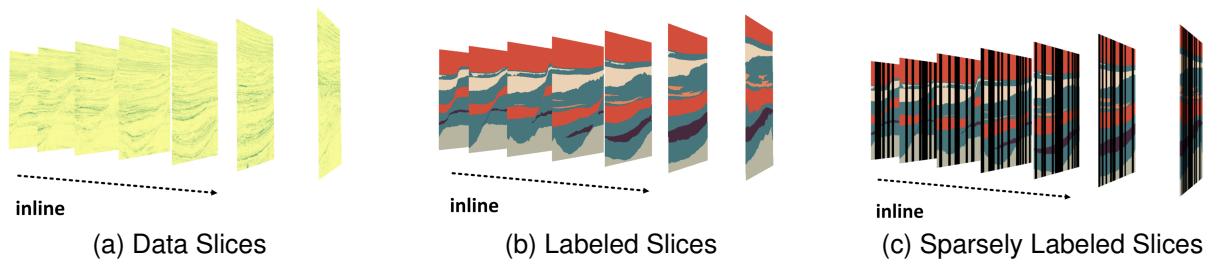


Fig. 7. The seismic data and corresponding labels are evenly sampled at equal step intervals as training data, and the step size is 100.

TABLE I  
Metrics of the SEAM AI survey.

Method	Class Accuracy							MCA	FWIOU	MIOU	F1
	PA	B/O	SMA	MTD	SMB	SV	SCS				
Sup w/o SDA (baseline)	94.84	99.03	94.52	86.55	97.52	63.37	88.00	88.17	90.34	82.45	89.69
Sup w/ SDA	94.79	98.20	95.21	80.00	98.15	60.65	86.88	86.52	90.23	81.48(-0.97)	88.95
ConSemiSup w/o SDA	93.55	96.71	95.49	79.61	96.03	55.07	81.73	84.11	88.12	78.25(-4.20)	86.62
SparseConSemiSup w/ SDA	96.62	98.22	96.06	91.07	98.69	76.95	94.63	92.60	93.55	87.56(+5.11)	92.99
ConSemiSup w/ SDA	96.72	98.56	96.16	91.64	98.69	74.77	94.73	92.43	93.74	<b>87.66(+5.21)</b>	93.03

TABLE II  
Metrics of Netherlands F3 survey.

Method	Class Accuracy							MCA	FWIOU	MIOU	F1
	PA	Upper	Middle	Low	R/C	Scruff	Zechstein				
Sup w/o SDA (baseline)	97.00	98.72	94.14	98.93	91.37	91.40	77.43	92.00	94.30	87.37	92.99
Sup w/ SDA	97.06	98.72	94.52	98.91	90.38	91.96	80.22	92.45	94.42	87.69(+0.32)	93.21
ConSemiSup w/o SDA	96.45	99.17	88.09	99.40	92.93	88.54	69.43	89.59	93.33	84.54(-2.83)	91.15
SparseConSemiSup w/ SDA	97.40	99.08	93.07	98.99	92.70	93.02	88.63	94.25	95.04	89.43(+2.06)	94.28
ConSemiSup w/ SDA	97.61	99.15	93.32	98.98	93.96	93.42	92.70	95.25	95.43	<b>90.83(+3.46)</b>	95.11

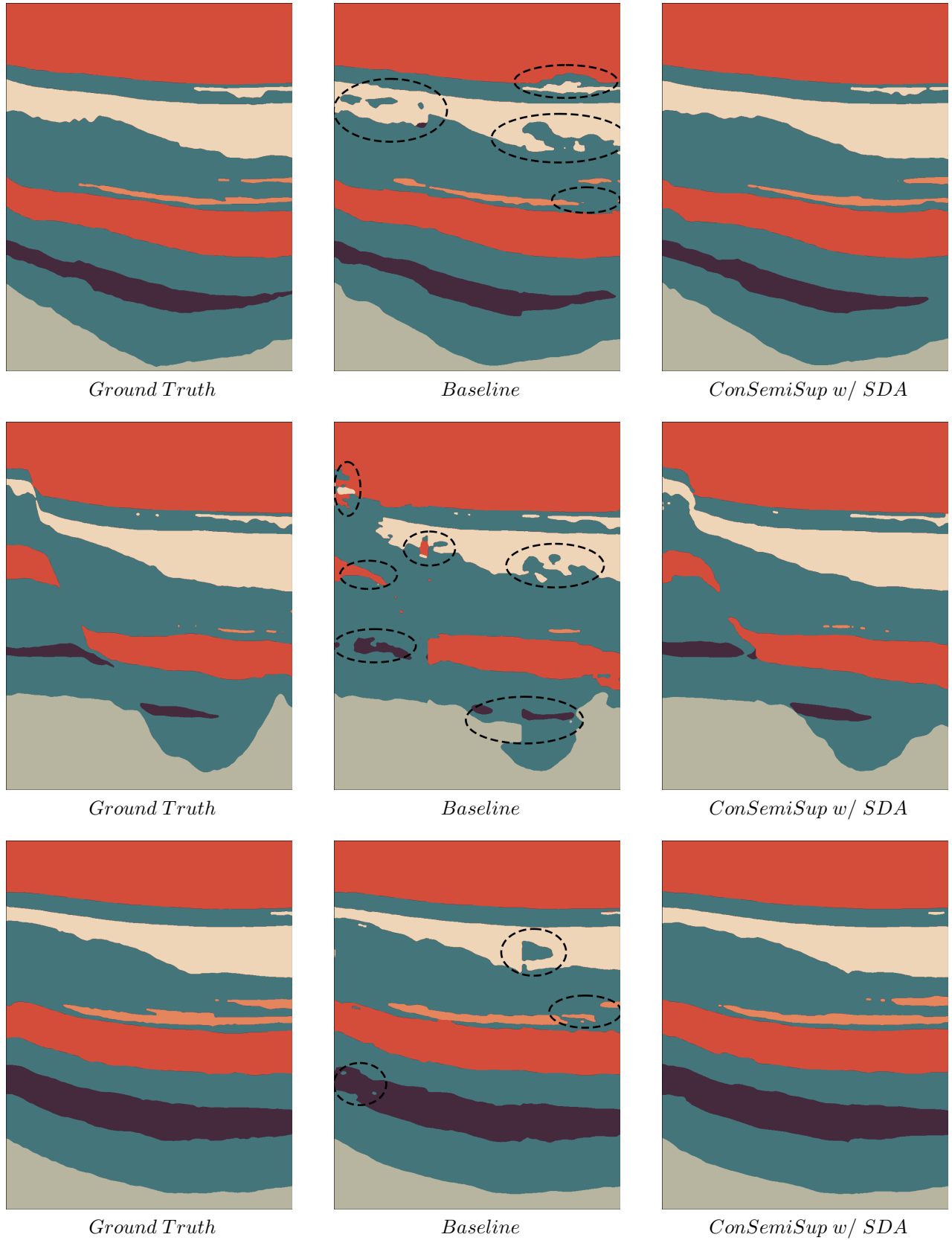


Fig. 8. The black dashed line delimits the regions of the classification confusion. On the SEAM AI survey, the semi-supervised method (right) with strong data augmentation significantly improves the fully supervised (center) prediction performance and increases the miou score by 5.21 points.



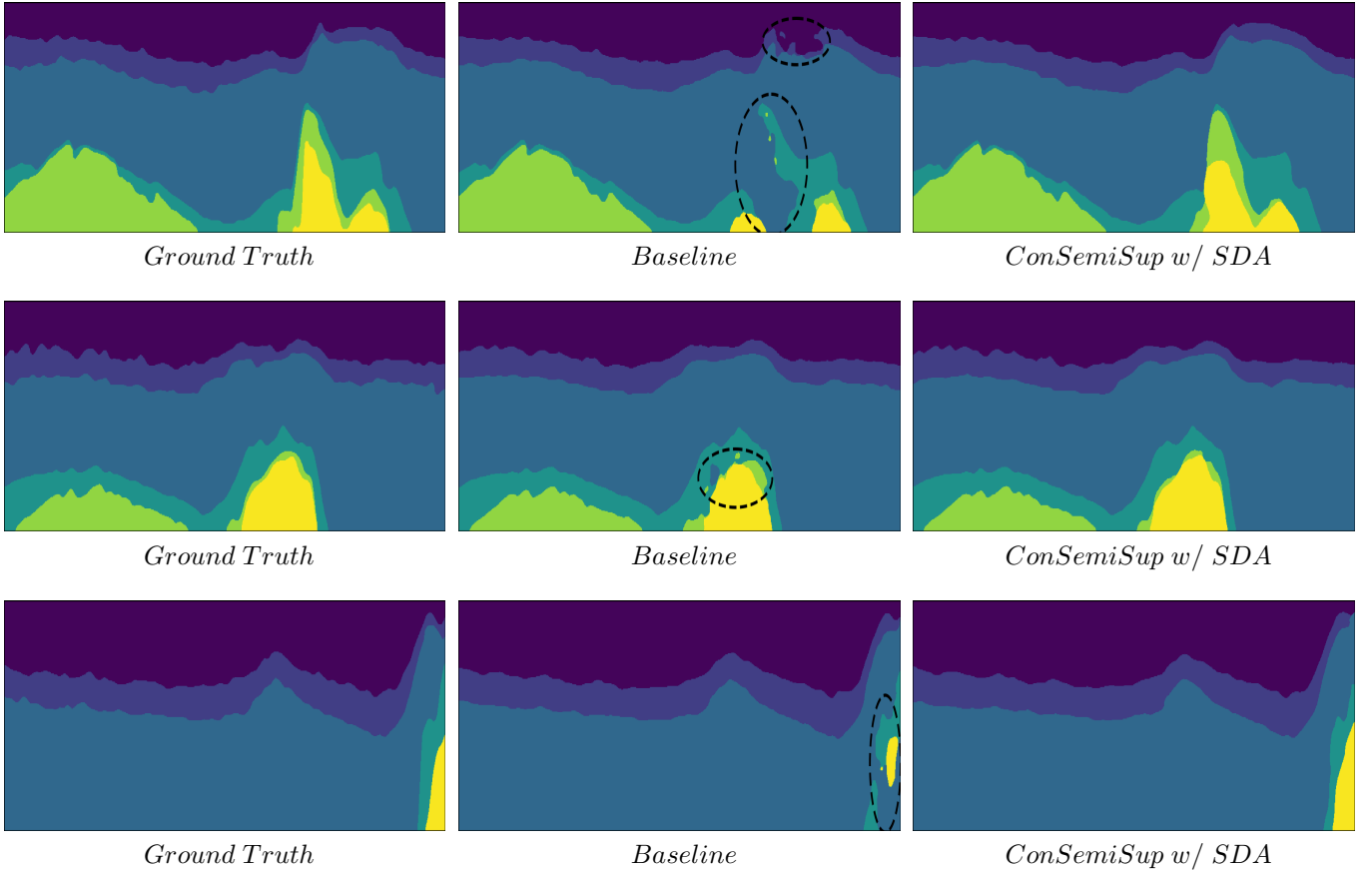


Fig. 9. On the Netherlands F3 survey, the miou score increases by 3.46 points, which is smaller than the SEAM AI survey. We believe that the reason for this difference is that only a few slices of seismic data contain all the seismic facies classes and most slices have only four classes, which would not be conducive to adequate comparison between the classes.

**Why SDA has a distinctly different role in fully and semi-supervised learning?** Different from simple transformations such as random rotation and horizontal flip, classmix and cutmix produce very violent disturbances to the semantic distribution of images, so they are called strong data augmentation (SDA). SDA disrupts the original data distribution, so that the features learned using pixel-level loss in fully supervised learning are not suitable for the original data distribution, so the model identification performance is degraded. Data augmentation is widely used in semi-supervised learning based on consistency regularization [8] [28] [39] [32] [21], which encourages the network to learn broader and fundamental semantic features in perturbed images. For seismic data, the distribution of seismic facies is strongly related to the depth of the stratum. If SDA is not used, the neural network may be able to achieve good results just by remembering the depth. Relying on this shortcut, the neural network fails to learn valuable seismic features, and the model will cause serious classification confusion when the seismic facies distribution changes significantly. We use SDA to properly disrupt the strong correlation between seismic facies distribution and depth, which is equivalent to increasing the learning difficulty of the network and encouraging the network to mine features in more seismic attributes instead of relying only on depth information.

#### IV. CONCLUSION

In order to alleviate the classification confusion of the trained model under a few labeled seismic facies slices, we propose a semi-supervised seismic facies identification method based on contrastive learning. Our semi-supervised method achieves very significant performance gains compared to fully supervised models. On more difficult tasks, even though the labels are sparse and incomplete, the model is still able to maintain a huge advantage. Moreover, our method can obtain a large number of negative samples without large batchsize and memory bank, enabling end-to-end training. We experimentally demonstrate the potential and effectiveness of contrastive learning in addressing classification confusion, as it can optimize the distribution of features across different seismic facies, resulting in a latent space with more distinguishable decision boundaries. Furthermore, our experiments can also demonstrate that SDA is crucial for semi-supervised seismic facies identification, which prevents the model from learning shortcuts and thus avoids model collapse, but SDA is irrelevant or even negatively affected for fully supervised learning. We expect that this work will bring some convenience to seismic interpreters and some enlightenment to peers in the geophysical community.

## ACKNOWLEDGMENTS

The authors are very indebted to the anonymous referees for their critical comments and suggestions for the improvement of this paper. This work was also supported by grants from the National Natural Science Foundation of China (Major Program, No.51991365), and the Natural Science Foundation of Shandong Province, China (No. ZR2021MF082).

## REFERENCES

- [1] Martin Wolf and Jacques Pelissier-Combes. “FACIOLOG-automatic electrofacies determination”. In: *SPWLA 23rd Annual Logging Symposium*. OnePetro. 1982.
- [2] Pierre Delfiner, Olivier Peyret, and Oberto Serra. “Automatic determination of lithology from well logs”. In: *SPE formation evaluation* 2.03 (1987), pp. 303–310.
- [3] Jeffrey L Baldwin, Richard M Bateman, and Chales L Wheatley. “Application of a neural network to the problem of mineral identification from well logs”. In: *The Log Analyst* 31.05 (1990).
- [4] Thierry Coléou, Manuel Poupon, and Kostia Azbel. “Unsupervised seismic facies classification: A review and comparison of techniques and implementation”. In: *The Leading Edge* 22.10 (2003), pp. 942–953.
- [5] Clare Elizabeth Bond et al. “What do you think this is? Conceptual uncertainty in geoscience interpretation”. In: *GSA today* 17.11 (2007), p. 4.
- [6] Laurens Van der Maaten and Geoffrey Hinton. “Visualizing data using t-SNE.” In: *Journal of machine learning research* 9.11 (2008).
- [7] Matthew D Zeiler et al. “Deconvolutional networks”. In: *2010 IEEE Computer Society Conference on computer vision and pattern recognition*. IEEE. 2010, pp. 2528–2535.
- [8] Mehdi Sajjadi, Mehran Javanmardi, and Tolga Tasdizen. “Regularization with stochastic transformations and perturbations for deep semi-supervised learning”. In: *Advances in neural information processing systems* 29 (2016).
- [9] Baochen Sun and Kate Saenko. “Deep coral: Correlation alignment for deep domain adaptation”. In: *European conference on computer vision*. Springer. 2016, pp. 443–450.
- [10] Liang-Chieh Chen et al. “Encoder-decoder with atrous separable convolution for semantic image segmentation”. In: *Proceedings of the European conference on computer vision (ECCV)*. 2018, pp. 801–818.
- [11] Haibin Di, Zhen Wang, and Ghassan AlRegib. “Deep convolutional neural networks for seismic salt-body delineation”. In: (2018).
- [12] Jesper S Dramsch and Mikael Luthje. “Deep-learning seismic facies on state-of-the-art CNN architectures”. In: *2018 SEG International Exposition and Annual Meeting*. OnePetro. 2018.
- [13] Weichang Li. “Classifying geological structure elements from seismic images using deep learning”. In: *2018 SEG International Exposition and Annual Meeting*. OnePetro. 2018.
- [14] Aaron van den Oord, Yazhe Li, and Oriol Vinyals. “Representation learning with contrastive predictive coding”. In: *arXiv preprint arXiv:1807.03748* (2018).
- [15] Zhirong Wu et al. “Unsupervised feature learning via non-parametric instance discrimination”. In: *Proceedings of the IEEE conference on computer vision and pattern recognition*. 2018, pp. 3733–3742.
- [16] Wei Xiong et al. “Seismic fault detection with convolutional neural network”. In: *Geophysics* 83.5 (2018), O97–O103.
- [17] Tao Zhao. “Seismic facies classification using different deep convolutional neural networks”. In: *2018 SEG International Exposition and Annual Meeting*. OnePetro. 2018.
- [18] Yazeed Alaudah, Motaz Alfarraj, and Ghassan AlRegib. “Structure label prediction using similarity-based retrieval and weakly supervised label mapping Structure label prediction”. In: *Geophysics* 84.1 (2019), pp. V67–V79.
- [19] Yazeed Alaudah, Moamen Soliman, and Ghassan Al-Regib. “Facies classification with weak and strong supervision: A comparative study”. In: *SEG Technical Program Expanded Abstracts 2019*. Society of Exploration Geophysicists, 2019, pp. 1868–1872.
- [20] Yazeed Alaudah et al. “A machine-learning benchmark for facies classification”. In: *Interpretation* 7.3 (2019), SE175–SE187.
- [21] Geoff French et al. “Semi-supervised semantic segmentation needs strong, varied perturbations”. In: *arXiv preprint arXiv:1906.01916* (2019).
- [22] Asghar Saleem et al. “Facies classification using semi-supervised deep learning with pseudo-labeling strategy”. In: *SEG International Exposition and Annual Meeting*. OnePetro. 2019.
- [23] Ting Chen et al. “A simple framework for contrastive learning of visual representations”. In: *International conference on machine learning*. PMLR. 2020, pp. 1597–1607.
- [24] Kaiming He et al. “Momentum contrast for unsupervised visual representation learning”. In: *Proceedings of the IEEE/CVF conference on computer vision and pattern recognition*. 2020, pp. 9729–9738.
- [25] Fangyu Li et al. “ADDCNN: An attention-based deep dilated convolutional neural network for seismic facies analysis with interpretable spatial-spectral maps”. In: *IEEE Transactions on Geoscience and Remote Sensing* 59.2 (2020), pp. 1733–1744.
- [26] Mingliang Liu et al. “Seismic facies classification using supervised convolutional neural networks and semi-supervised generative adversarial networks”. In: *Geophysics* 85.4 (2020), O47–O58.
- [27] Xingye Liu et al. “Facies identification based on multikernel relevance vector machine”. In: *IEEE Transac-*

- tions on Geoscience and Remote Sensing 58.10 (2020), pp. 7269–7282.
- [28] Qizhe Xie et al. “Unsupervised data augmentation for consistency training”. In: *Advances in Neural Information Processing Systems* 33 (2020), pp. 6256–6268.
- [29] Yimin Dou et al. “Attention-Based 3-D Seismic Fault Segmentation Training by a Few 2-D Slice Labels”. In: *IEEE Transactions on Geoscience and Remote Sensing* 60 (2021), pp. 1–15.
- [30] Runhai Feng et al. “Bayesian convolutional neural networks for seismic facies classification”. In: *IEEE Transactions on Geoscience and Remote Sensing* 59.10 (2021), pp. 8933–8940.
- [31] Shikun Liu et al. “Bootstrapping semantic segmentation with regional contrast”. In: *arXiv preprint arXiv:2104.04465* (2021).
- [32] Viktor Olsson et al. “Classmix: Segmentation-based data augmentation for semi-supervised learning”. In: *Proceedings of the IEEE/CVF Winter Conference on Applications of Computer Vision*. 2021, pp. 1369–1378.
- [33] Xintao Chai et al. “An Open-Source Package for Deep-Learning-Based Seismic Facies Classification: Benchmarking Experiments on the SEG 2020 Open Data”. In: *IEEE Transactions on Geoscience and Remote Sensing* 60 (2022), pp. 1–19.
- [34] Xiaoyu Chen et al. “A Stronger Baseline for Seismic Facies Classification With Less Data”. In: *IEEE Transactions on Geoscience and Remote Sensing* 60 (2022), pp. 1–10.
- [35] Yimin Dou et al. “MD Loss: Efficient Training of 3-D Seismic Fault Segmentation Network Under Sparse Labels by Weakening Anomaly Annotation”. In: *IEEE Transactions on Geoscience and Remote Sensing* 60 (2022), pp. 1–14.
- [36] Kiran Kokilepersaud, Mohit Prabhushankar, and Ghasan AlRegib. “Volumetric supervised contrastive learning for seismic semantic segmentation”. In: *Second International Meeting for Applied Geoscience & Energy*. Society of Exploration Geophysicists and American Association of Petroleum ... 2022, pp. 1699–1703.
- [37] M Quamer Nasim et al. “Seismic facies analysis: a deep domain adaptation approach”. In: *IEEE Transactions on Geoscience and Remote Sensing* 60 (2022), pp. 1–16.
- [38] Yuchao Wang et al. “Semi-Supervised Semantic Segmentation Using Unreliable Pseudo-Labels”. In: *Proceedings of the IEEE/CVF Conference on Computer Vision and Pattern Recognition*. 2022, pp. 4248–4257.
- [39] Lihe Yang et al. “St++: Make self-training work better for semi-supervised semantic segmentation”. In: *Proceedings of the IEEE/CVF Conference on Computer Vision and Pattern Recognition*. 2022, pp. 4268–4277.
- [40] Hao Zhang et al. “SaltISCG: Interactive Salt Segmentation Method Based on CNN and Graph Cut”. In: *IEEE Transactions on Geoscience and Remote Sensing* 60 (2022), pp. 1–14.

## APPENDIX

We give the results of ablation experiment to find optimal hyperparameter settings in the appendix to facilitate code reproducibility. Furthermore, latent space visualization provides intuitive evidence for the effectiveness of our method.

## LATENT SPACE VISUALIZATION

To intuitively understand the role of contrastive learning, we visualize the latent space features of the fully-supervised and semi-supervised models on the two seismic surveys, respectively. As can be seen in Figure (10), there is severe entanglement between the features of different classes of the fully supervised model, while the semi-supervised method produces sharper decision boundaries.

## HYPERPARAMETER ABLATION EXPERIMENT

We conduct ablation experiments for learning rate (Tab.III), temperature coefficient (Tab.IV), confidence threshold (Tab.V), and smooth factor (Tab.VI).

TABLE III

The - means that the model cannot converge at this learning rate.

$lr$	$10^{-1}$	$10^{-2}$	$10^{-3}$	$10^{-4}$	$10^{-5}$
SEAM AI	-	-	<b>87.66</b>	85.83	81.24
Netherlands F3	71.11	88.39	90.45	<b>90.83</b>	80.76

TABLE IV

Temperature coefficient.

$\tau$	0.01	0.1	0.5	1	10
SEAM AI	86.50	87.18	<b>87.66</b>	87.51	86.97
Netherlands F3	89.46	90.52	90.41	<b>90.83</b>	89.51

TABLE V  
Confidence threshold.

$t_w$	0.6	0.6	0.7	0.7
$t_s$	0.8	0.85	0.9	0.95
SEAM AI	87.35	87.65	<b>87.66</b>	87.64
Netherlands F3	90.04	89.44	89.50	<b>90.83</b>

TABLE VI  
Smooth factor.

$\epsilon$	0	0.1	0.2	0.3
SEAM AI	87.03	<b>87.66</b>	87.49	82.89
Netherlands F3	89.57	<b>90.83</b>	89.31	86.83

## MORE EXPERIMENTS

The following experiments (Tab.VII) (Tab.VIII) demonstrate that our method improves performance by contrastive learning from unlabeled data, and not because the contrastive loss for labeled data is computed or BN layers records features from

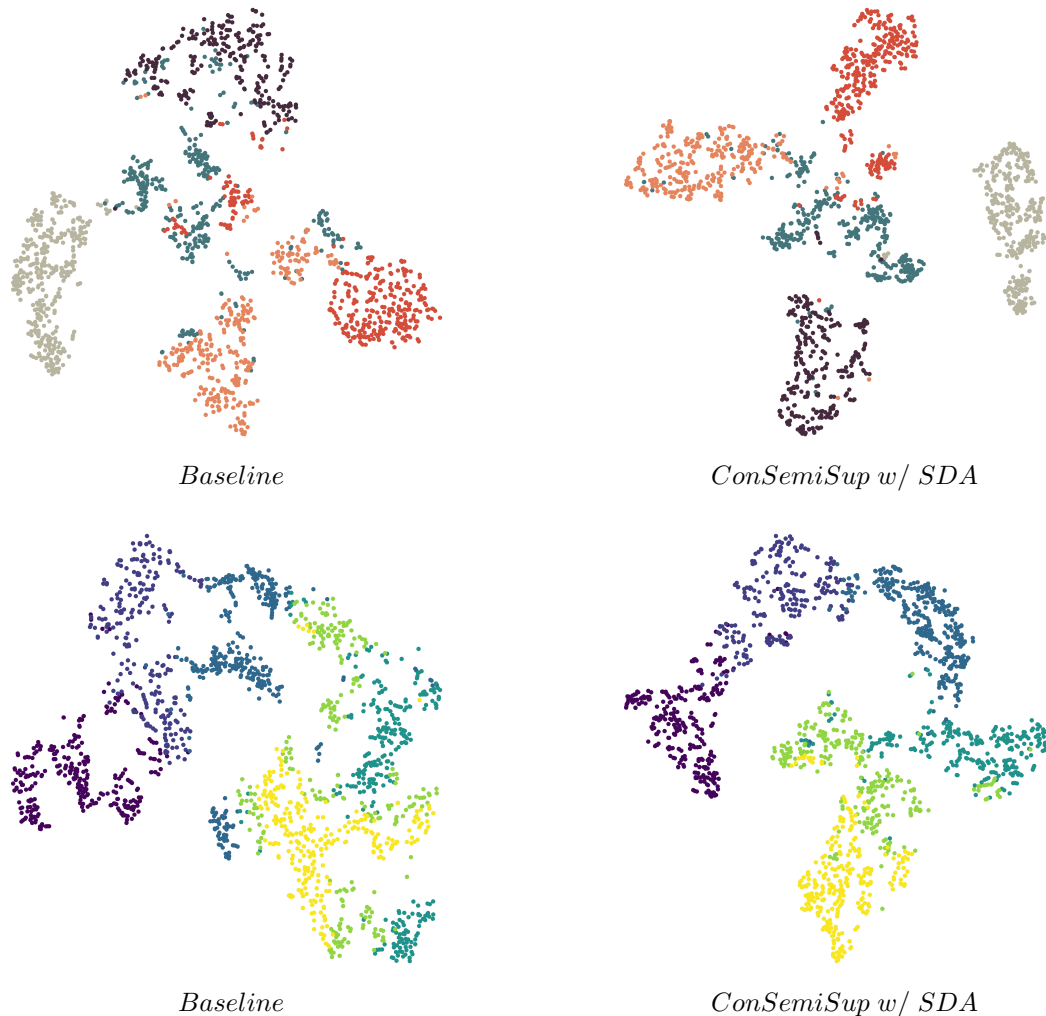


Fig. 10. Visualization of the latent space learned by *Baseline* and *ConSemiSup w/ SDA*, using t-SNE [6]. Contrastive semi-supervised model enhances cohesion of seismic facies features of the same class and reduces the bias in the features of the same class.

unlabeled data in the forward process. The experimental results of the last two lines also prove that the performance gain from the momentum encoder (ema) is small and even the momentum encoder can adversely affect the model, so we can drop the momentum encoder to save graphics memory and training time.

TABLE VII  
SEAM AI survey.

labeled data	unlabeled data	$\mathcal{L}_{sup}$	$\mathcal{L}_{con}$	ema	MIOU
✓		✓			82.45
✓		✓	✓		82.78
✓	✓	✓			81.70
✓	✓	✓	✓		87.66
✓	✓	✓	✓	✓	<b>87.94</b>

TABLE VIII  
Netherlands F3 survey.

labeled data	unlabeled data	$\mathcal{L}_{sup}$	$\mathcal{L}_{con}$	ema	MIOU
✓		✓			87.37
✓		✓	✓		88.95
✓	✓	✓			87.83
✓	✓	✓	✓		<b>90.83</b>
✓	✓	✓	✓	✓	90.21